LARGE EDDY SIMULATION OF HEATED PULSED JETS IN HIGH SPEED TURBULENT CROSSFLOW

A Thesis
Presented to
The Academic Faculty

by

Venkata-Ramya Pasumarti

In Partial Fulfillment
of the Requirements for the Degree
Master of Science in
Aerospace Engineering

School of Aerospace Engineering
Georgia Institute of Technology
December 2010

LARGE EDDY SIMULATION OF HEATED PULSED JETS IN HIGH SPEED TURBULENT CROSSFLOW

Approved by:

Professor Suresh Menon, Advisor
School of Aerospace Engineering
Georgia Institute of Technology

Professor Jerry Seitzman
School of Aerospace Engineering
Georgia Institute of Technology

Professor Jeff Jagoda
School of Aerospace Engineering
Georgia Institute of Technology

Date Approved: 22 July 2010

ACKNOWLEDGEMENTS

I am sincerely thankful to my advisor Dr. Suresh Menon, for his valuable support and guidance throughout the course of my stay here at Computational Combustion Lab. My discussions with him have been a constant source of motivation and an enormous learning experience for me. I would like to thank my committee members, Dr. Jerry Seitzman and Dr. Jeff Jagoda. This work would not have been complete without their constructive criticism and continuous guidance. I would also like to express my gratitude to Pratt & Whitney for their financial support.

My thanks are due to current and past CCL colleagues: Dr. Franklin Genin, Dr. Baris Ali Sen, Dr. Kaushik Balakrishnan, Dr. Jung Choi, Dr. Srikant Srinivasan, Kalyana Gottiparthi, Andy Smith, Tim Gallagher, Orcun Kozaka, Leandro Gryngarten, Satoshi Ukai and Chaitanya Ghodke who helped me understand the models and code used in the lab. I owe a very special thanks to Matthieu Masquelet and Joey Schulz, who have taken the extra effort to guide me during times of need, and to Anuradha Sanyal, who has been a close confidant and a friend.

My acknowledgements will not be complete without thanking my close friends, Sivakumar Harikumar and Vrishank Raghav, for making my stay in Atlanta very memorable. I also want to thank my dearest friend Deepthi Cheboli, who has always been there to guide and cheer me. Expressions of gratitude are not sufficient to thank Sameer Indarapu. Our interactions over the years have been the most reliable source of support that I've ever had, and I dedicate my success to him.

Finally, I would like to thank my parents, Sudhakar Pasumarti and Devi Pasumarti, and my sister, Divya Pasumarti for always believing in me. I am ever indebted to them for all their love and support.

TABLE OF CONTENTS

LIST OF TABLES

LIST OF FIGURES

SUMMARY

The jet-in-crossflow problem has been extensively studied, mainly because of its applications in film cooling and injector designs. It has been established that in low-speed flows, pulsing the jet significantly enhances mixing and jet penetration. This work investigates the effects of pulsing on mixing and jet trajectory in high speed (compressible) flow, using Large Eddy Simulation. Jets with different density ratios, velocity ratios and momentum ratios are pulsed from an injector into a crossflow. Density ratios used are 0.55 (CH_4/air), 1.0 (air/air) and 1.5 (CO_2/air). Results are compared with the low speed cases studied in the past and then analyzed for high speed scaling. The simulations show that the lower density jet develops faster than a higher density jet. This results in more spreading for the lower density jet. Scaling for jet spread and the decay of centerline jet concentration for these cases are established, and a variable density scaling law is developed and used to predict jet penetration in the far field.

In most non-premixed combustor systems, the fuel and air being mixed are at different initial temperatures and densities. To account for these effects, heated jets at temperatures equal to 540K and 3000K have been examined. It has been observed that, in addition to the lower density of heated jets, the higher kinematic viscosity effects the jet penetration. This effect has been included and validated in the scaling law for the jet trajectory.

CHAPTER I

INTRODUCTION

The fluid dynamics of a perpendicularly injected jet of fluid into turbulent and laminar crossflows has been extensively studied and hence has become a canonical problem in the study of fluid mechanics. The reason for this owes to applications, such as fuel injectors, cooling of combustion gases in gas turbines, film cooling in turbomachinery and discharge of chimney gases into air, whose governing physical phenomenon are related to the jet in crossflow problem. The 'jet in crossflow' is one of the simplest injector design for efficient fuel and oxidizer mixing in non-premixed combustion systems [11]. An understanding of the physics of this problem requires a characterization of the jet penetration, entrainment and mixing with the crossflow.

Complex instantaneous flow fields and certain characteristic vortical structures have consistently been observed in steady jet in crossflow configurations (fig 1). Some of these vortical structures have also been observed in pulsed jets [8, 29, 17]. The interface between the high speed pulse and the low speed recirculation region ahead of the pulse, and between the high speed pulse and the wake region after the pulse consists of the jet shear layer. Counter rotating vortex pairs are formed in the plume region and are responsible for enhanced mixing. Horse shoe vortices, that are formed due to the interaction of the incoming turbulent crossflow boundary layer and the pulse, are found close to the injector and do not influence mixing. Lastly, wake vortices, which form in between the boundary layer and the plume region, can be seen downstream of the injector. As will be shown later, all the above structures have been identified in the current high speed pulsed jet simulations with intense fluctuations as well.

Typically, two distinct regions can be identified in a transverse jet: the near field and

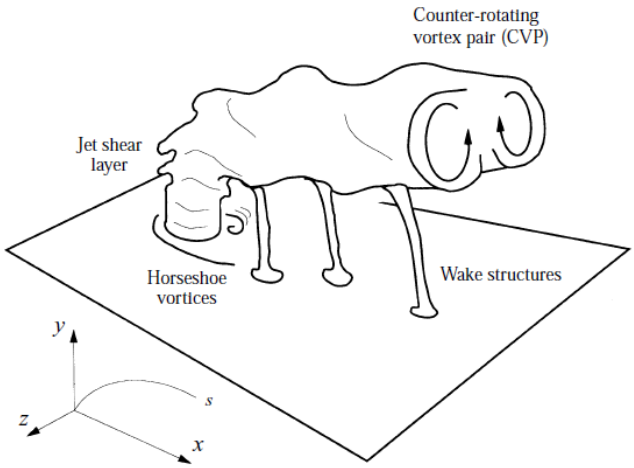

Figure 1: Representation of the vortical structures in the wake region of a steady transverse jet in crossflow by Fric and Roshko [9] . Reproduced from Smith and Mungal [30]

the far field [17]. The near field region consists of the potential core (where the jet is nearly uniform in velocity and concentration) and the transition region (where the jet deflects substantially). The far field is characterized by counter rotating, streamwise vortices, which affect the jet trajectory. Several attempts [31, 30, 1] were made to obtain a scaling law for the jet trajectories in the near and far field regions. Smith and Mungal [30] identified three different length scales for different regions of the transverse jet : d, rd and r^2d. In general, the jet trajectory is expressed as [17]

$$\frac{y}{rd} = A\left(\frac{x}{rd}\right)^m \tag{1}$$

where d is the nozzle diameter and r is the jet-to-crossflow velocity ratio, $r = U_j/U_{cf}$. A and m are experimentally determined constants, which take different values depending on the definition of jet trajectory. In the case of variable density flows, it is customary to define r as the square root of the momentum flux ratio [30]:

$$r = \left(\frac{\rho_j U_j^2}{\rho_{cf} U_{cf}^2}\right)^{1/2} \tag{2}$$

While steady jets have been extensively studied, recent experiments [8, 29, 21, 32] on pulsed jets have shown characteristics that are drastically different than for steady

jets. A distinct vortex loop merging pattern is observed around a steady round jet in crossflow. As the jet is pulsed, the vortex loops are stretched and distorted. This causes certain parts of the neighboring loops of opposite or same vorticity signs to merge, resulting in cancelation or intensification of vorticity [8]. As a result, pulsed jets can penetrate up to 5 times deeper into the crossflow than a steady jet [18]. This makes them a promising engineering approach for fuel injectors.

1.1 Jet Structure and Mixing

An experimental study [8] of a pulsed, round jet revealed that the structure and strength of the vortex rings generated by a fully modulated square pulse in a crossflow is governed by the pulsing frequency (for a fixed jet and crossflow combination). Short injection times create vortex ring structures whereas long injection times generate axially elongated turbulent puffs [18]. As the vortex rings become more distinct, the mixing and hence the penetration depth increases. Smaller duty cycles, square wave excitation (as opposed to sinusoidal excitation) and lower pulsing frequencies contribute to increased jet penetration [23, 18, 15]. These experiments have played a key role in qualitatively describing vortex rings. Simulating this flow would give a better understanding of the dynamics and mixing characteristics of the fluids.

The mixing rates, jet structure and penetration are strongly influenced by several flow parameters (jet to crossflow momentum ratio, jet Reynolds number, Strouhal number). This requires a study of the optimum pulsing conditions that increase jet penetration and concurrently enhance jet mixing. Johari *et al.* [18] predicted that the optimal jet penetration occurs for duty cycles as low as 20%.

High amplitude acoustic pulsation in a transverse jet was studied by Vermeulen *et al.* [32, 33]. They observed a significant increase in entrainment and size of the vortex rings found in the near field of the jet. For a fixed jet-to-crossflow momentum ratio,

the size and strength of the vortex rings also depend on the stroke ratio, $\frac{L}{d}$. The stroke length, L of a pulse is given by

$$L = \frac{1}{A}\int_0^\tau \int_A u_j dA dt = \bar{U_j}\tau \tag{3}$$

where τ is the temporal width of the pulse. In other words, for a time period $T = 1/f$ of the pulse, τ is the time for which the pulse is 'on'. Hence, the stroke ratio is in turn related to the duty cycle of the pulse ($\alpha = \tau/T$) through Strouhal number by [28]

$$\frac{L}{d} = \frac{\alpha}{St} \tag{4}$$

Here, α is the duty cycle of the pulse. Physically, if the pulses were coming out of a piston (or from an injector as in the experiments), the stroke ratio is equivalent to the 'push' given to each pulse. The pulse width τ and the spatial separation (quantified by the duty cycle α) govern the interaction among the successive flow structures. This effect on the near field structure of the jet in turn changes the far-field jet penetration. Based on the stroke ratio, the structure of each pulse can be identified as a compact vortex ring, a vortex puff and a turbulent puff [17]. Richards [26] defines a 'puff' as a 'strongly turbulent mass of fluid moving through surroundings with which they readily mix'. For a stroke length less than $4d$, the pulses created are distinct and compact vortex rings whereas, for a stroke length in the range of, $4d < L \leq 20d$, the jet splits into two streams, a deep penetrating vortex puff and a trailing jet of fluid [17]. For similar reasons, vortex rings with a small stroke ratio contain lesser momentum giving rise to interactions in the near field. This decreases the jet penetration. On the other hand, vortex rings with very high stroke ratio give rise to a trailing column of vorticity, which interact with subsequent structures in the near field.

Vortex rings with a small stroke ratio contain less momentum, causing interactions in the near field. This decreases the jet penetration. On the other hand, vortex rings

with very high stroke ratio result in a trailing column of vorticity, which interacts with subsequent structures in the near field. This dependance of jet penetration on the stroke ratio was studied by Rajes *et al.* [28]. They develop a classification map (fig 2) of ring velocity ratio and Stroke ratio to predict an optimal curve for the pulsing characteristics, which would give the maximum jet penetration.

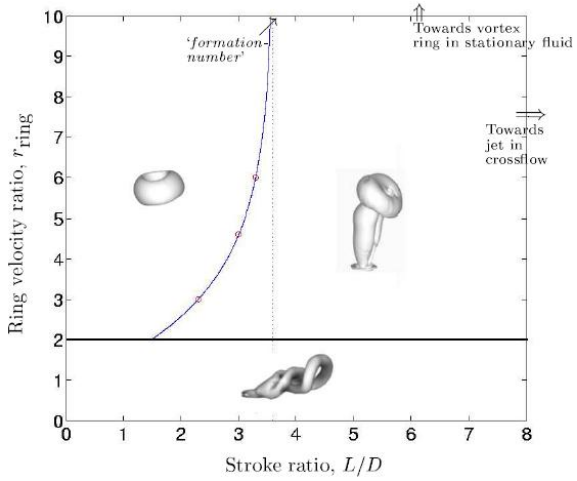

Figure 2: Classification map showing different entrainment characteristics for vortex rings in different flow regimes . Reproduced from Sau and Mahes [28]

1.2 Trajectory and Scaling

There are several ways to define the jet trajectory. Smith and Mungal [30] define the jet trajectory as the locus of the maximum scalar concentration, while Kamotani and Greber [19] and Johari *et al.* [17] define it as the locus of the maximum velocity. For brevity, most studies on the trajectory of fully modulated jets are done by using self similar scaling of turbulent puffs and vortex rings in quiescent media [17, 28].

The path taken by the jet depends on the interaction between flow structures, which makes the trajectory a strong function of the stroke ratio and duty cycle of the pulse. The scaling law (in the self-similar region) for a uniform-density pulsed jet in an

incompressible crossflow is given by [17]

$$\frac{y - y_o}{d} = k \left(r_p \frac{L}{d} \right)^{1/4} \left(\frac{x}{d} \right)^{1/4} \tag{5}$$

where $r_p = \bar{U}_j / U_{cf}$, is the jet-to-crossflow velocity defined based on the average jet velocity during the pulse, and k is an experimentally determined constant that includes other flow properties such as viscosity and inflow profile. Although certain aspects of this problem have been studied experimentally, not much work has been done to understand the change in the physics of this problem under a wide range of conditions.

1.3 Effect of Heating

In many non-premixed combustor systems, the fuel and air mix at different initial temperatures and densities. Mixing of jet air into hot, fuel-rich products of a gas turbine (i.e., quenching) is a critical step in a RQL combustor. Cooling combustion gases in gas turbine combustors is typically done by injecting relatively cool air through holes in the surrounding walls. Most of these applications rely on rapid and thorough mixing of the fluids. The change in jet penetration and mixing due to pulsing of a cold jet in a hot confined crossflow was studied in detail by Vermeulen *et al.* [32, 33]. They have observed a decrease in the jet spread for increasing pulsing frequencies. In addition, they obtained an optimum Strouhal number for maximum jet mixing and predicted at least a 100% increase in the jet penetration. However, these optimizations were only made for a single set of initial conditions Predicting the mixing effectiveness and temperature profiles for different initial conditions would help in a better understanding of the effect of jet temperature on the mixing rates.

Much less information is available on heated jet behavior. Callaghan and Ruggeri [2, 3] correlate temperature distributions in the symmetry plane of the jet, while the experiments of Ramsey and Goldstein [25] obtained the velocity and temperature profiles in the cross-section as well as the symmetry planes, for small momentum

ratios. Callaghan *et al.* [3] investigated the physics behind a heated-air jet directed perpendicularly into an air stream, by conducting wind tunnel experiments. They use simple dimensional analysis involving known variables to obtain:

$$\frac{y}{d} = f\left(\frac{\rho_j U_j d}{\mu_j}\right)\left(\frac{\rho_j}{\rho_{cf}}\right)\left(\frac{\mu_j}{\mu_{cf}}\right)\left(\frac{x}{d}\right) \tag{6}$$

From the measurements of the penetration depth for heated jets in crossflow, an experimental fit for the scaling law was obtained, as a function of the mass flux ratio (as opposed to momentum flux ratio) :

$$\left(\frac{y}{d}\right) = 1.6\left(\frac{\rho_j}{\rho_{cf}}\right)^a\left(\frac{U_j}{U_{cf}}\right)^b\left(\frac{x}{d}\right)^{0.26} \tag{7}$$

where $0.2 < a, b < 0.8$. This observation is explained in further detail in the current study. Steady heated jets have been studied in detail by Kamotani *et al.* [19]. They have observed that, in addition to velocity, the jet trajectory can be a function of temperature. In addition, not only is the velocity trajectory observed to be higher than that for temperature, but the temperature trajectory also depends on density ratio [19].

1.4 Compressibility Effects

Most of the experimental results discussed above have been limited to low-speed incompressible flows. The nature of compressible turbulence differs from its incompressible behavior. The subgrid closure used in Large-Eddy Simulation (LES) needs to be adapted to the modeling of compressibility effects of turbulent flows [11]. In this case, in addition to the solenoidal component (which is typical of incompressible flows), turbulent velocity is composed of a dilational part. The closure of the energy equation plays a key role in compressible flows. Modeling of the compressible part of the dissipation term is discussed by Genin [11] and is used in this work.

1.5 Objectives

The aim of this study is to investigate the behavior of high speed pulsed jets at variable jet and cross-flow densities using LES. The predicted scaling rules are evaluated against the classical low-speed rules, and then further redefined or extended to high-speed and variable density flows. In addition, we also study the passive scalar mixing characteristics and the effect of inflow turbulence on the small and large scale mixing of the jet and the crossflow. Specifically, the following objectives are identified:

1. Obtain scaling laws to predict the jet trajectory for variable density flows.

   An analytic scaling law for a uniform density pulsed jet in crossflow has been proposed by Johari *et al.* [17]. However, these earlier studies have focussed on very low-speed jets and cross-flow (of the order of 1-10 m/s) and hence, the flow was essentially incompressible. The low speed studies were essentially necessary due to the experimental requirements but is not very practical in terms of application. Much higher speed cross flow (of the order of $100m/s$) and appropriately proportional jet velocity (or alternatively, high momentum flows) are more realistic for fuel injector applications [24]. However, there is not much information of jet penetration and mixing in such high speed flows. This study aims at obtaining and validating the variable density scaling laws.

2. Study the effects of turbulence intensity, jet-to-crossflow momentum ratio and pulsing parameters on the jet trajectory in high speed crossflows.

   Although certain aspects of this problem have been studied experimentally, not much work has been done to understand the change in the physics of this problem under a wide range of conditions. A fundamental question of interest is to see how the scaling rules and sensitivity of penetration depth to frequency,

stroke duty cycle and velocity (or momentum) ratio changes with increase in the magnitude of the flow speed. Another related issue is how these earlier low-speed (essentially constant density) studies scale with variable density (e.g., due to preheating, change in jet species, etc).

3. Analyze the effect of pulsing on scalar dissipation. Obtain the optimum operating conditions for efficient temperature mixing.

   Though it has been well established that pulsing enhances jet mixing and penetration significantly, little work has been done to analyze its effects on the temperature profiles for heated jets. Temperature fluctuations couple with the effects of pulsing to further change the jet trajectory. Quantifying this effect would help understand the fluid dynamics of heated jets better.

This thesis is organized as follows. In the next section the LES formulation and the problem setup is given. This is followed by results and conclusions, with experimental comparisons, discussions on high speed flow features, variable density scaling law validation and passive scalar mixing. Finally, heated jets are studied and the effect of high temperature on the scaling laws is analyzed. The paper concludes by summarizing the major findings of this study.

CHAPTER II

FORMULATION

The numerical scheme (LES) solves the unsteady, compressible conservation equations. The flow variables are separated into resolved and unresolved (sub-grid scale) components by a spatial filtering operation (i.e., $f = \tilde{f} + f''$) [24]. Favre filtering is defined as $\tilde{f} = \overline{\rho f}/\bar{\rho}$, where the overbar represents spatial filtering. This averaging procedure significantly reduces the number of unclosed terms in compressible turbulence. The following filtered conservation equations are solved.

$$\frac{\partial \bar{\rho}}{\partial t} + \frac{\partial \bar{\rho}\widetilde{u}_j}{\partial x_j} = 0 \tag{8}$$

$$\frac{\partial \bar{\rho}\widetilde{u}_i}{\partial t} + \frac{\partial}{\partial x_j}\left[\bar{\rho}\widetilde{u}_i\widetilde{u}_j + \bar{p}\delta_{ij} - \bar{\tau}_{ij} + \tau_{ij}^{sgs}\right] = 0 \tag{9}$$

$$\frac{\partial \bar{\rho}\widetilde{E}}{\partial t} + \frac{\partial}{\partial x_i}\left[\left(\bar{\rho}\widetilde{E} + \bar{p}\right)\widetilde{u}_i + \bar{q}_i - \widetilde{u}_j\bar{\tau}_{ji} + H_i^{sgs} + \sigma_i^{sgs}\right] = 0 \tag{10}$$

$$\frac{\partial \bar{\rho}\widetilde{Y}_k}{\partial t} + \frac{\partial}{\partial x_i}\left[\bar{\rho}(\widetilde{Y}_k\widetilde{u}_i + \tilde{Y}_k\widetilde{V_{i,k}}) + Y_{i,k}^{sgs} + \theta_{i,k}^{sgs}\right] = 0 \quad k = 1, N_s \tag{11}$$

where variables with overbar denotes spatially filtered quantities, and variables with tilde denote Favre filtered quantities. Here, ρ is the density, u_i are the velocity components in Cartesian coordinates, E is the total energy per unit of mass, p is the pressure, and Y_k is mass fraction. The filtered total energy is given as the sum of the filtered internal energy $\tilde{e}$, the resolved kinetic energy $(1/2)[\tilde{u}_i\tilde{u}_i]$, and the subgrid kinetic energy $k^{sgs} = (1/2)[\widetilde{u_iu_i} - \tilde{u}_i\tilde{u}_i]$

Calorifically perfect assumption is made in employing the equation of state, as the current problem deals with moderate temperatures and pressures. Filtered pressure, density and temperature are related by $\bar{p} = \bar{\rho}R\widetilde{T} + T^{sgs}$, where R is the gas constant. The filtered energy per unit mass is $\tilde{e} = c_\nu\tilde{T}$ and the filtered internal enthalpy $\tilde{h}$ is defined as $\tilde{h} = \tilde{e} + \bar{p}/\bar{\rho}$ (can be expressed as $\tilde{h} = c_p\tilde{T}$ for a perfect gas). The ratio of

specific heats, $\gamma = c_p/c_\nu$ is assumed to be a constant ($\gamma = 1.4$). The filtered strain rate is used to compute the filtered viscous stress tensor $\bar{\tau}_{i,j}$ and Sutherland law is used to estimate the viscous coefficient, μ. The filtered heat-flux vector $\bar{q}_i$ is computed from the Fourier law. Prandtl number is assumed to be a constant ($Pr = 0.72$), and is used to obtain the thermal conductivity. Modeling of these terms is briefly summarized below.

The modeled *subgrid-scale* terms are denoted with a superscript 'sgs'. These are the subgrid stress tensor $\tau_{i,j}^{sgs} = \bar{\rho}(\widetilde{u_i u_j} - \tilde{u}_i\tilde{u}_j)$, the subgrid enthalpy flux $H_i^{sgs} = \bar{\rho}(\widetilde{Eu_i} - \tilde{E}\tilde{u}_i) + (\overline{u_i P} - \tilde{u}_i\bar{p})$, subgrid viscous work, $\sigma_i^{sgs} = (\overline{u_j\tau_{i,j}} - \tilde{u}_j\overline{\tau_{i,j}})$, and the subgrid diffusive flux of passive scalar $Y_i^{sgs} = \bar{\rho}(\widetilde{u_i Y} - \tilde{u}_i\tilde{Y})$.

2.1 Subgrid Closure Model

A closure based on the transport model for the subgrid kinetic energy k^{sgs} is used for the subgrid momentum and energy fluxes. The subgrid kinetic energy is obtained by solving the following transport equation along with the LES Eqs (8)-(11).

$$\frac{\partial \bar{\rho} k^{sgs}}{\partial t} + \frac{\partial}{\partial x_i}\left(\bar{\rho}\widetilde{u}_i k^{sgs}\right) = P^{sgs} - D^{sgs} + \frac{\partial}{\partial x_i}\left(\frac{\bar{\rho}\nu_t}{Pr_t}\frac{\partial k^{sgs}}{\partial x_i}\right) \tag{12}$$

where ν_t is the turbulent viscosity and Pr_t is the turbulent Prandtl number (assumed constant), P^{sgs} is the subgrid kinetic energy production, and D^{sgs} is the subgrid kinetic energy dissipation. These three terms can be written as follows:

$$\nu_t = C_\nu \sqrt{k^{sgs}}\,\overline{\Delta} \tag{13}$$

$$P^{sgs} = -\tau_{ij}^{sgs}\frac{\partial \widetilde{u}_i}{\partial x_j} \tag{14}$$

$$D^{sgs} = C_\epsilon \bar{\rho}\frac{\sqrt{(k^{sgs})^3}}{\overline{\Delta}} \tag{15}$$

where the model coefficients C_ν and C_ϵ in Eqs (13) and(15) are evaluated dynamically, based on the localized dynamic k^{sgs} model (LDKM) [20]. The subgrid stresses, energy

flux and species diffusion are closed with ν_t computed from (13) as follows [10]:

$$\tau_{ij}^{sgs} = -2\bar{\rho}\nu_t\left(\widetilde{S}_{ij} - \frac{1}{3}\widetilde{S}_{kk}\delta_{ij}\right) + \frac{2}{3}\bar{\rho}k^{sgs}\delta_{ij} \quad (16)$$

$$H_i^{sgs} + \sigma_i^{sgs} = -(\bar{\rho}\nu_t + \mu)\frac{\partial k^{sgs}}{\partial x_i} - \frac{\bar{\rho}\nu_t}{Pr_t}\frac{\partial \tilde{T}}{\partial x_i} + \tilde{u}_j\tau_{ij}^{sgs} \quad (17)$$

$$Y_{i,k}^{sgs} = -\frac{\bar{\rho}\nu_t}{Sc_t}\frac{\partial \tilde{Y}_k}{\partial x_i} \quad (18)$$

The remaining terms such as T^{sgs}, are neglected. Past studies [24, 4] have shown this to be a good approximation.

2.2 Localized Dynamic Closure for Subgrid Model Coefficients

The closure terms in the LES and k^{sgs} equations have four model coefficients $(c_\nu, c_\epsilon, Pr_t, \alpha_{pd})$. A dynamic evaluation of these coefficients, c_ν and c_ϵ, is based on the framework of the localized dynamic k^{sgs} model (LDKM) [20]. Constant values, based on previous results, are assumed for Pr_t and α_{pd}. Noting $\langle f \rangle$, the application of an explicit top-hat test filter of size $\hat{\Delta}$ ($\hat{\Delta} > \bar{\Delta}$) on variable f, the Leonard stress at the test-filter level is defined as

$$L_{ij} = \langle \bar{p} \rangle \left(\frac{\langle \bar{\rho}\tilde{u}_i\tilde{u}_j \rangle}{\langle \bar{\rho} \rangle} - \frac{\langle \bar{\rho}\tilde{u}_i \rangle}{\langle \bar{\rho} \rangle}\frac{\langle \bar{\rho}\tilde{u}_i \rangle}{\langle \bar{\rho} \rangle} \right) \quad (19)$$

The LDKM uses the experimentally observed similarity between τ_{ij}^{sgs} and L_{ij} and assumes a similarity between L_{ij} and $< \tau_{ij}^{sgs} >$, so that L_{ij} can be expressed at the test-scale level as

$$L_{ij} = -2\,\langle \bar{\rho} \rangle\, c_\nu \sqrt{k^{test}}\hat{\Delta}\left(\frac{\left\langle \bar{\rho}\widetilde{S_{ij}} \right\rangle}{\langle \bar{\rho} \rangle} - \frac{1}{3}\frac{\left\langle \bar{\rho}\widetilde{S_{kk}} \right\rangle}{\langle \bar{\rho} \rangle}\delta_{i,j} \right) + \frac{2}{3}\,\langle \bar{\rho} \rangle\, k^{test}\delta_{i,j} \quad (20)$$

where k^{test} is the trace of the Leonard stress tensor. Here, c_ν is the only unknown and can be estimated using a least squares method as

$$c_\nu = -\frac{M_{ij}L'_{ij}}{2M_{ij}L_{ij}} \tag{21}$$

where $M_{ij} = \sqrt{k^{test}}\hat{\Delta}(\left\langle \bar{\rho}\widetilde{S_{ij}} \right\rangle - \frac{1}{3}\left\langle \bar{\rho}\widetilde{S_{kk}} \right\rangle \delta_{i,j})$ and $L'_{ij} = L_{ij} - \frac{2}{3}\langle\bar{\rho}\rangle\, k^{test}\delta_{i,j}$.

The transport equation for the kinetic energy at the test-scale level is similar to k^{sgs}, governed by production, diffusion, dissipation, and pressure-dilation correlation at the test-scale level. These terms are functions of the resolved variables and of the subgrid stresses only. Under the similarity assumption, the dissipation of k^{test}, $D_{k^{test}} = \hat{\bar{\rho}}c_\epsilon(k^{test})^{3/2}/\hat{\Delta}$ where, again, only the closure coefficient remains unknown. The coefficient c_ϵ is then determined as

$$\begin{aligned} c_\epsilon = \; & \frac{\hat{\Delta}}{\langle\bar{\rho}\rangle(k^{test})^{\frac{3}{2}}}((\mu+\mu_t)\left[\left\langle\widetilde{\Sigma_{i,j}}\frac{\partial\tilde{u_j}}{\partial x_i}\right\rangle - \frac{1}{\langle\bar{\rho}\rangle}\left\langle\widetilde{\Sigma_{i,j}}\right\rangle\left\langle\bar{\rho}\frac{\partial\tilde{u_j}}{\partial x_i}\right\rangle\right] - \\ & \frac{2}{3}\left[\left\langle\bar{\rho}k^{sgs}\frac{\partial\tilde{u_k}}{\partial x_k}\right\rangle - \frac{1}{\langle\bar{\rho}\rangle}\langle\bar{\rho}k^{sgs}\rangle\left\langle\bar{\rho}\frac{\partial\tilde{u_k}}{\partial x_k}\right\rangle\right]) \end{aligned} \tag{22}$$

where $\tilde{\Sigma_{i,j}} = 2(\tilde{S_{ij}} - \frac{1}{3}\tilde{S_{kk}}\delta_{i,j})$. This expression models both solenoidal and dilational dissipations together using the same closure expression. This approximation remains valid as long as the turbulent Mach number remains small (i.e., far from unity), so that dilational dissipation remains very small. It should be notes that for most supersonic flow applications, the turbulent Mach number is small, and the dilational dissipation is negligible compared to the solenoidal dissipation.

The dynamic evaluation if c_ν and c_ϵ has been validated and applied to many low-speed applications. For compressible flows simulations, the energy field also plays an important role in the flow evolution.

2.3 Problem Setup

The LES governing Eqs (8)-(12), are solved using a block-structured finite-volume hybrid scheme developed and well validated in the past [20]. The hybrid scheme uses a fourth-order accurate central scheme to resolve regions without discontinuities

and smoothly switches to a high-order flux-difference splitting method in regions of high gradients and discontinuities. The algorithm has been validated and applied for various applications elsewhere [12]. The algorithm is implemented in a multi-block framework in the distributed computing LES solver using the Message Passing Interface (MPI) library for parallel communications over the spatially decomposed domain.

Figure 4(a) shows a schematic of the geometry for the pulsed jet in crossflow simulation. The domain spans $20d$ in the axial direction, $16d$ in the normal direction and $13d$ in the spanwise direction. The sensitivity of the predictions to the domain size was addressed earlier and the extent of the domain used here is sufficient to allow comparison with experimental data and to capture all the physical processes in regions of interest, without the influence of the walls. Air is injected through a pipe of diameter, $d = 3.98mm$. The incoming jet velocity is prescribed at a distance, $1.0d$ below the flat plate, to allow for the flow to develop naturally into the crossflow. A similar approach was used earlier [22]. Figure 4(b) shows the jet exit velocity profile at the point A in Figure 4(a). The temporary reversal in the jet direction during the pulse 'off' time is due to the low pressure created by switching 'off' the pulse. This behavior in the velocity profiles have been observed in the experimental studies of Shapiro *et al.* [29], and in the DNS studies of Sau *et al.* [27].

The crossflow has been modeled as a reasonably realistic turbulent channel inflow. Fig. 3 shows the schematic of the inflow turbulence setup used. A uniform isotropic box of turbulent fluctuations is initially generated and allowed to evolve to realistic turbulence at an appropriate Re_λ (228.2) until we obtained the required Re_λ. The resulting flow field is interpolated into the channel grid and the fluctuations are scaled to suit a turbulent channel boundary layer profile. The resulting fluctuations are then dynamically added to the inflow at every time step with a superimposed rms profile

and added to the mean flow, which is prescribed by a sixth-power turbulent channel boundary layer profile with sufficient grid resolution in the turbulent boundary layer ($\sim$ 16 points).

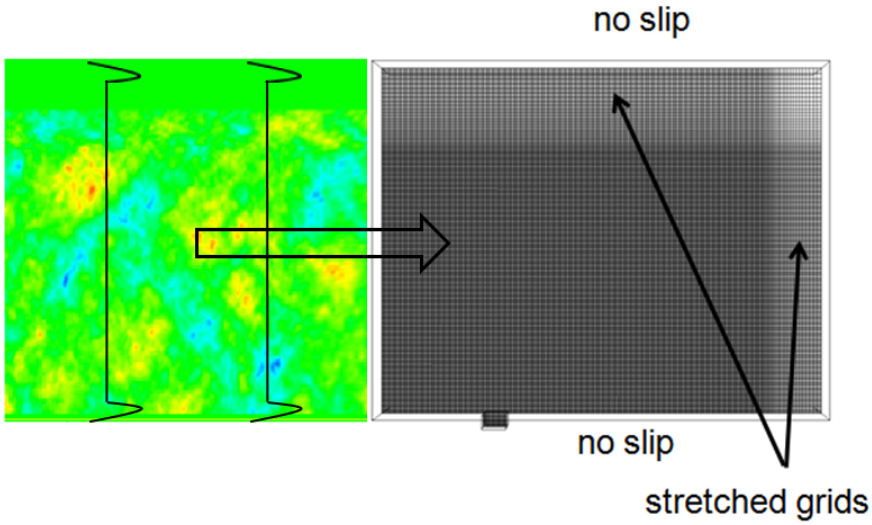

Figure 3: Figure on the left shows the box of isotropic turbulence, which is scaled and added onto the channel crossflow. Figure on the right shows the front view of the grid used in the jet in crossflow domain.

The jet inflow profile has been prescribed by a sixth-power turbulent boundary layer profile. Past DNS studies of steady jets in crossflow by Suman *et al.* [31] show that the effect of jet inlet velocity profile on the jet penetration and trajectory is small for higher jet to crossflow velocity ratios. The velocity ratios used in this study are considered high, as in Suman *et al.*[31], and therefore, the current inflow specification is considered reasonable. No-slip boundary conditions on the top and bottom walls and symmetry conditions in the spanwise direction are enforced in the domain. The inflow and outflow are treated with characteristic boundary conditions. Sponge conditions are used to damp the numerical reflections at the outflow boundary in the x direction. [16].

The domain is discretized by a total of 10.8 million grid cells, with 438 grid points

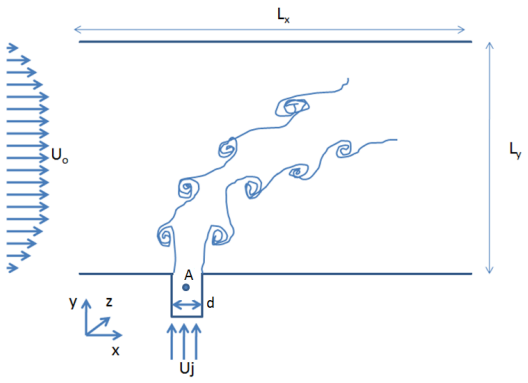

(a)

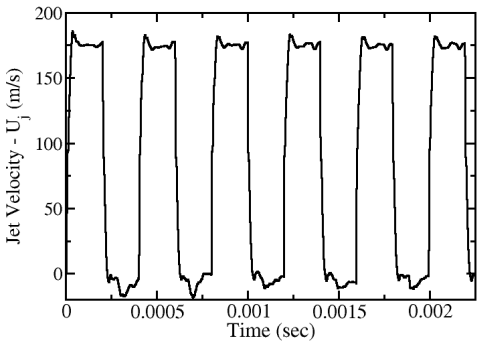

(b)

Figure 4: (a) Geometry for the pulsed jet in crossflow simulation. Injector diameter, $d = 4\ mm$, $L_x = 80\ mm$, $L_y = 60\ mm$ (b) Pulsed jet velocity profile observed at point A in (a).

in x direction, 259 grid points in the y direction and 96 points in the z direction. The grid is uniform and clustered near the injector and the wake region, and stretches towards the outflow. The height of the first cell from the lower wall is approximately $\Delta y^+ = 4.38$, when scaled by the friction velocity of channel flow. Grid independence study has been performed using a range of grids earlier. A finer grid of $628 \times 260 \times 112$ cells, with the first point corresponding to $\Delta y^+ = 2.92$, showed overall similar results and therefore the former grid is used for all the reported results. Near wall resolution is not very high here, but the focus is on the jet penetration away from the wall and therefor, the present near wall grid is considered adequate for the current grid.

Analysis of the flow also shows realistic inertial range range turbulence in the chosen

grid. Figure 5 shows the energy spectra in the jet shear and wake region of the flow. It is observed that the inertial range follows -5/3 scaling in the resolved scale, suggesting a reasonable grid for LES. As expected there is a peak at 2500 Hz, which is the pulsing frequency used for this case.

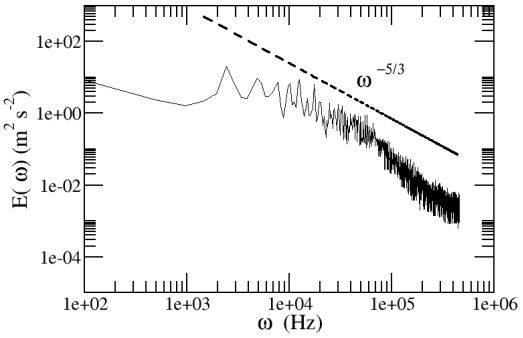

(a)

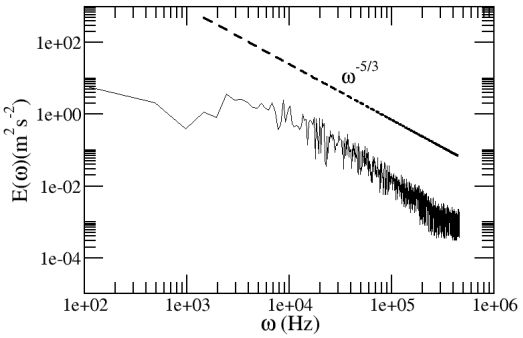

(b)

Figure 5: Spectra of the turbulent kinetic energy at two locations in the centerplane. (a) Along the developing shear layer - in the near field. (b) In the wake of the jet.

CHAPTER III

RESULTS AND DISCUSSION

Jet penetration and mixing are the two main aspects of the study. Jet penetration is defined here as the locus of the maximum velocity. We use the experimental studies of Eroglu *et al.* [8] to compare the statistically averaged penetration of the jet, at different frequencies. For all the cases, the crossflow velocity is maintained at 50 m/s. The initial conditions used are summarized in Table 1 below. The velocity (r), mass flux (MR) and momentum ratios (J) are defined as

$$r = U_j/U_{cf} \qquad MR = \rho_j U_j/\rho_{cf} U_{cf} \qquad J = \rho_j U_j^2/\rho_{cf} U_{cf}^2 \tag{23}$$

where subscripts j and cf denote jet and crossflow fluids. Cases 1-6 are used for comparing the jet penetration depths to the low speed experimental results of Eroglu *et al.* [8]. The jet to crossflow velocity ratio is maintained at $r = 4.4$, and Strouhal numbers of 0, 0.04, 0.07, 0.11, 0.17 and 0.3 are used. Note that the stroke ratios given in Table 1 for Case 1-6 correspond to the respective Strouhal numbers. Case 7 with an air jet is used as the reference case. Cases 8-11 use CH_4 and CO_2 jets to study the effect of the jet to crossflow density ratio, ρ_j/ρ_{cf}. The density ratios given in Table 1 are the ratios of the corresponding molecular weights at room temperature. Cases 8 and 9 maintain the same jet to crossflow velocity ratio and Strouhal number as case 7, which allows for the validation of the variable density scaling law for jet penetration. Cases 10 and 11 adjust the jet to crossflow velocity ratios, to have the same momentum ratio and the Strouhal number as Case 7. These cases are used to compare the changes in jet concentration decay and jet spread, when the jet trajectory is the same. In other words, these cases let us focuses on the effect of jet to crossflow density ratio. Cases 12 and 13 are air jets that maintain the same jet-to-crossflow

Table 1: Summary of the flow conditions used for the pulsed jet in crossflow simulations.

Case	Jet	ρ_j/ρ_{cf}	r	MR	J	L/d	St
1 - 6	Air	1.0	4.4	4.4	19.36	-, 12.5, 7.1, 4.5, 2.9, 1.6	0, 0.04, 0.07, 0.11, 0.17, 0.3
7	Air	1.0	4.0	4.0	16.0	10.0	0.05
8	CH_4	0.554	4.0	2.22	8.86	10.0	0.05
9	CO_2	1.52	4.0	6.08	24.32	10.0	0.05
10	CH_4	0.554	5.37	2.97	16.0	10.0	0.05
11	CO_2	1.52	3.24	4.93	16.0	10.0	0.05
12	Air	0.554 (T_{cf}/T_j)	4.0	2.22	8.86	10.0	0.05
13	Air	0.1 (T_{cf}/T_j)	4.0	0.4	1.6	10.0	0.05

velocity ratio as the reference Case 7, which have a lower density due to higher jet temperature. These cases are used to validate the heated jet variable density scaling law.

3.1 Comparison with Low Speed Results

The statistically averaged jet penetration data collected at two different x locations is compared with the low speed experimental work of Eroglu *et al.* [8]. Figure 6 shows the variation of normalized jet penetration (y/d) as a function of the Strouhal number at $x/d = 3$ and $x/d = 10$. As seen in the figure, there is a fairly good agreement with the experiments. A sharp increase in the jet penetration, compared to steady jets is noticed. Since the jet velocity and the jet diameter are constant, a change in Strouhal number directly translates to a change in the pulsing frequency ($St = fd/U_j$). Jets with very high pulsing frequency gives rise to strongly interacting vortices. For a sufficiently high frequency, the behavior of the pulsed jet is close to that of a steady jet. This is the reason we see jet penetration comparable to a steady jet and a jet with $St = 0.3$ in Fig. 6. In addition, this trend also indicates that there is an optimal pulsing frequency at which a maximum jet penetration is observed. It

should be noted that the domain has been extended to $y = 22d$ in the y-direction, to account for the jet penetration in Cases 2,3 and 4.

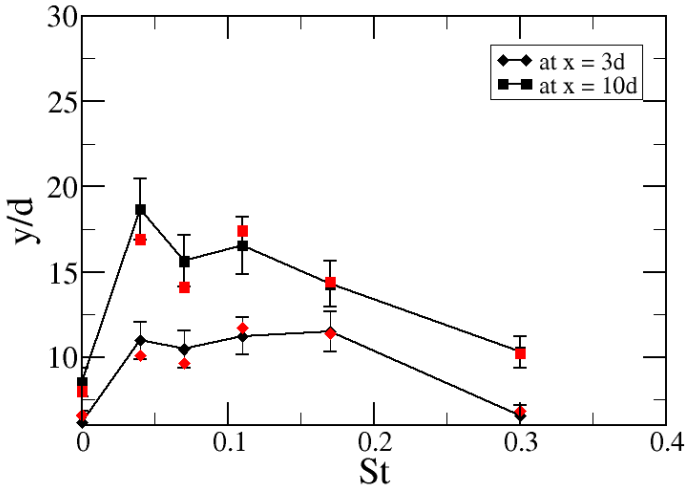

Figure 6: Penetration depth variation with Strouhal number for $r = 4.4$. Black points are from experiments [8]. Red points are from the simulation (Case 1).

3.2 Flow Features in the High Speed Cases

Three distinct regions can be observed from the instantaneous vorticity profiles of the jet at a quasi-steady state. The 'core' region is where the jet pushes forward through the crossflow. In this region, the velocity of the jet is maximum and the vortex rings are distinct. The jet-crossflow interaction begins in the 'transition' region (at around $y = 4 - 5d$) and the jet starts bending over. Finally, the 'self-similar' region is where the jet trajectory can be predicted using a scaling law. For low speed flows, the jet is much more structured. Visualizations from the low speed and low frequency experiments of Eroglu *et al.* [8] and Shapiro *et al.* [29] show slight distinction between consecutive vortices even in the far field. The current work deals with high speed turbulent crossflow and high speed jets. Due to this, vortices in the near field and far field interact rapidly with the inflow turbulence and the turbulent boundary layer.

This results in quicker breakdown of the vortices giving rise to small scale structures.

Figure 7 shows instantaneous contours of the magnitude of vorticity in the symmetry plane. Cases 1-6, with decreasing pulsing frequencies are shown here. The structure of the initial vortex obtained is a strong function of the jet to crossflow velocity ratio and the stroke ratio, L/d. Sau and Mahesh [27] obtain a classification map showing the dynamics of vortex rings in a crossflow. For a stroke ratio greater than 4 (and a velocity ratio greater than 2), they predict that the vortices with an entrainment (as opposed to distinct puffs) are obtained. A similar trend can be observed in Fig. 7. In Figs. 7(a) and 7(b), the stroke ratio is less than 4.0, giving rise to distinct, non-interacting vortices in the near field. In Figs 7(c), 7(d) and 7(e), the initial vortex causes significant entrainment and interacts with neighboring vortices in the near field itself. The interaction between the jet shear layer in the near field and the turbulent boundary layer is also observed. Two distinct branches can be observed for the jet - one that penetrates deep into the crossflow and one that is formed in the wake as a result of interaction with the crossflow boundary layer. Between pulses, the boundary layer entrains part of the jet shear layer giving rise to stronger and wider wake structures (compared to the wake vortices with a laminar low speed crossflow).

Figure 15 shows the process of vortex merging in the near field for Case 6 ($St = 0.3$). The vortex ring formed in the near field is in the form of a distinct puff and does not have fluid entrained behind it. In this case, the merging pattern of the vortices is much simpler. Fig 15(a) shows the windward and leeward sides of the first two vortex rings. As the pulses are injected into the crossflow, the leeward side of the vortex ring stretches out of its plane, and merges with the windward vortex of the earlier pulse. This merging results in cancellation of vortices of opposite sign. The remaining parts of the ring spiral into a counter-rotating vortex pair, as shown in

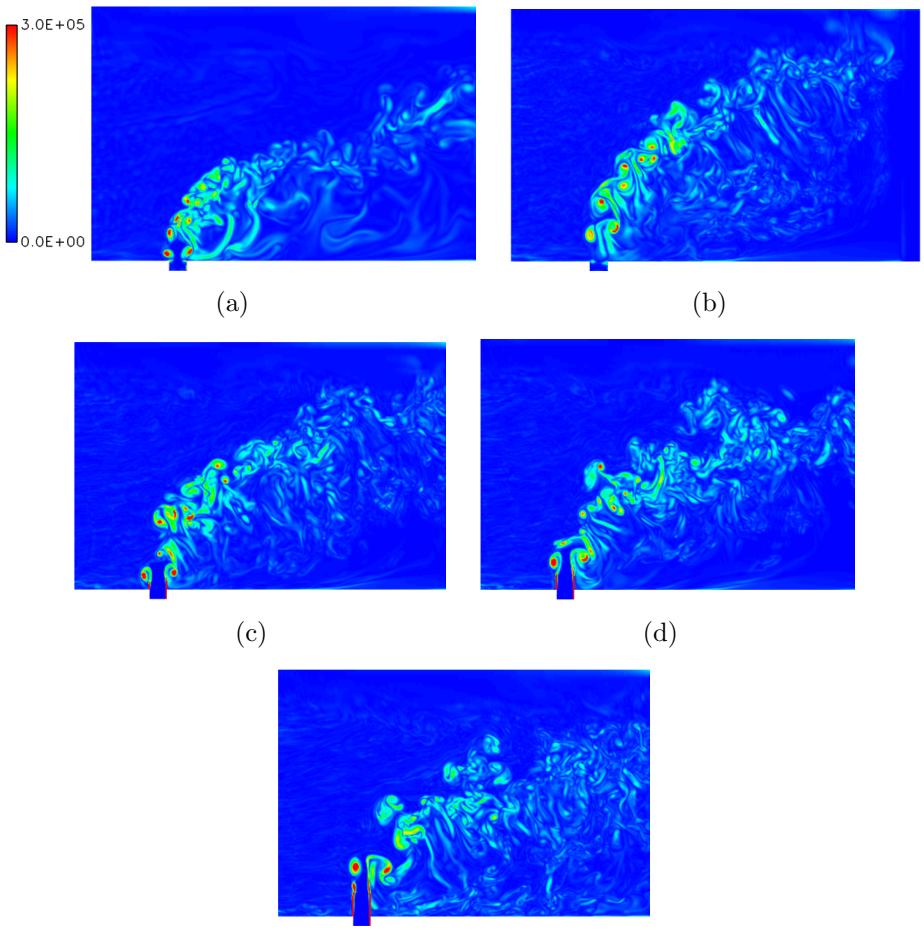

Figure 7: Contours of vorticity magnitude in the symmetry plane. (a) $St = 0.3$, $L/d = 1.6$ (b) $St = 0.17$, $L/d = 2.9$ (c) $St = 0.11$, $L/d = 4.5$ (d) $St = 0.07$, $L/d = 7.1$ (e) $St = 0.04$, $L/d = 12.5$

Fig. 8(f).

The merging pattern is slightly different for vortex rings with a trailing jet of fluid. Figure 9 shows the merging pattern for Case 4 ($St = 0.11$). Figure 9(a) shows the initial vortex ring with an entrainment. This trailing fluid separates from the vortex ring as seen in Fig. 9(b) and 9(c). The leeward side of the second vortex pulse initially merges with the separated trailing edge before merging with windward side of the first pulse (Fig. 9(c) - 9(e)). This process is repeated with the consecutive pulses (Fig. 9(f))

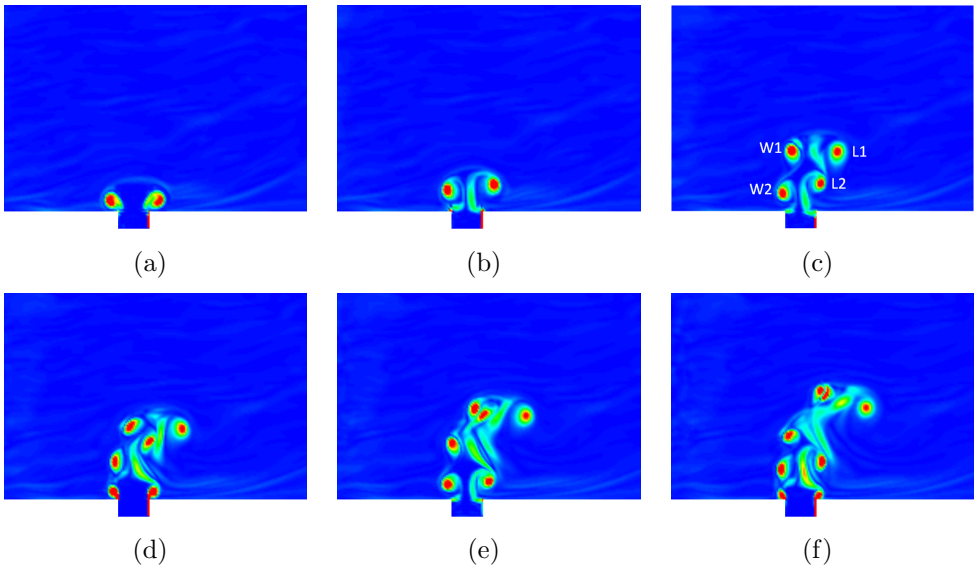

Figure 8: Contours of vorticity magnitude in the symmetry plane, for Case 6 ($St = 0.3$). Contour scale is the same as in Fig. 7. In Fig. 15(c), W and L indicate the windward and leeward side of the pulses and 1 and 2 indicate the first and the second pulse.

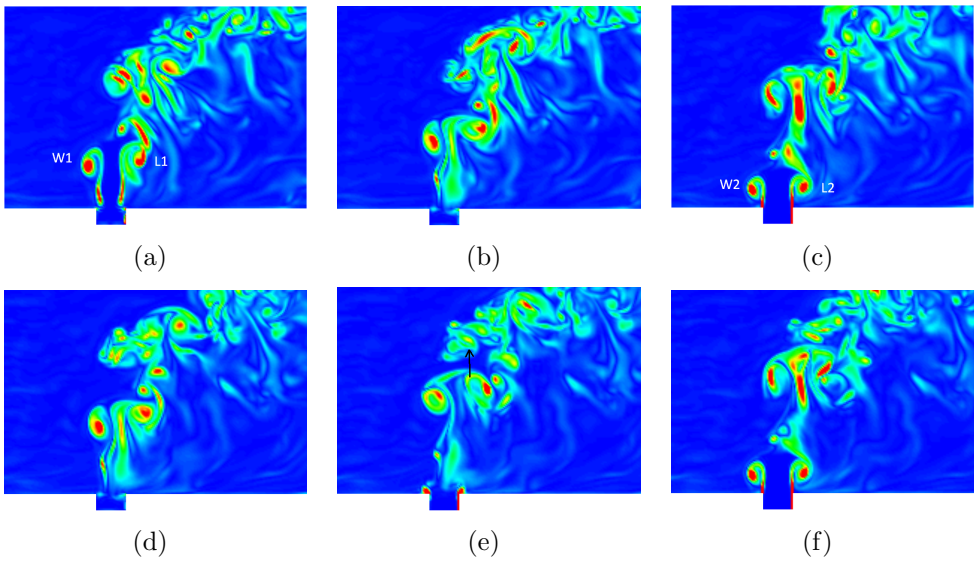

Figure 9: Contours of vorticity magnitude in the symmetry plane, for Case 4 ($St = 0.11$). Contour scale is the same as in Fig. 7.

The second invariant of the velocity gradient tensor, Q is well suited for vortex identification [6]. An isosurface of positive Q highlights the regions dominated by vorticity of strain ($Q-$ criterion) is shown in Fig. 10. Figure 10(a) shows the vortex breakup pattern due to the interaction of the first vortex with the turbulent boundary

layer. This, is once again, a result of the high speeds involved. Each vortex ring that is formed is distorted out of its plane such that the downstream part of the ring stretches to merge with the upstream part of the neighboring ring. This is a result of the high speed flows simulated here. The remaining parts of the ring spiral into a counter-rotating vortex pair, as observed in Fig. 10(b).

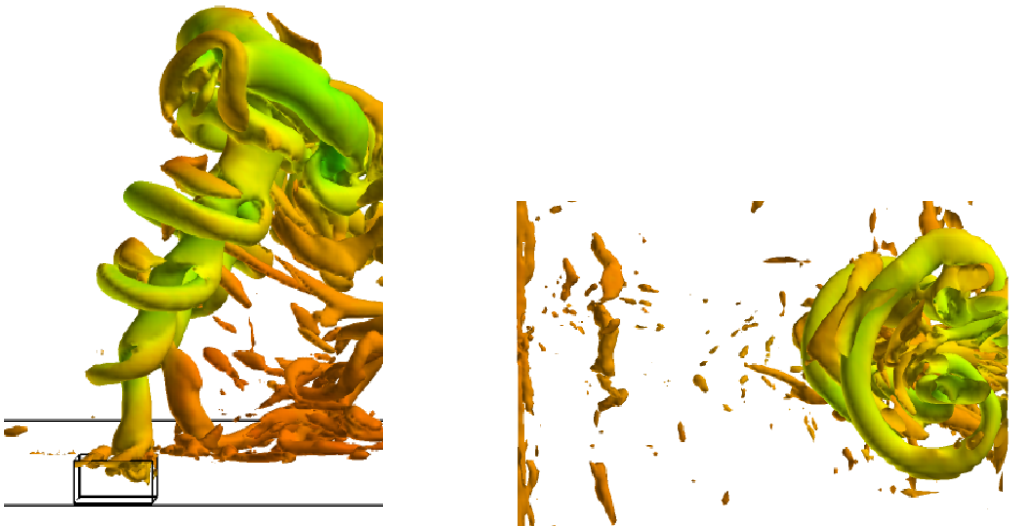

(a) (b)

Figure 10: Iso-surface of $Q = 10^8 s^{-2}$, colored with a density scalar (a) Vortex breakdown and formation in the near field (b) Top view of the counter-rotating vortex pair formation in the plume region (top view).

3.3 Jet Trajectory and Scaling

Grid independence has been studied by comparing the jet penetration of the current and a finer grid (described earlier). As can be seen (Fig. 11), the current and the finer grid predict comparable jet penetration, suggesting grid independence.

For a steady jet in crossflow, it has been well established that the jet structure and trajectory depend primarily on the jet to crossflow momentum ratio, J. In the case of a pulsed jet in crossflow, in addition to the momentum ratio, parameters such as St and frequency, can play role in determining the near-field structure, and hence the far field trajectory. A variable density scaling law must account for these additional

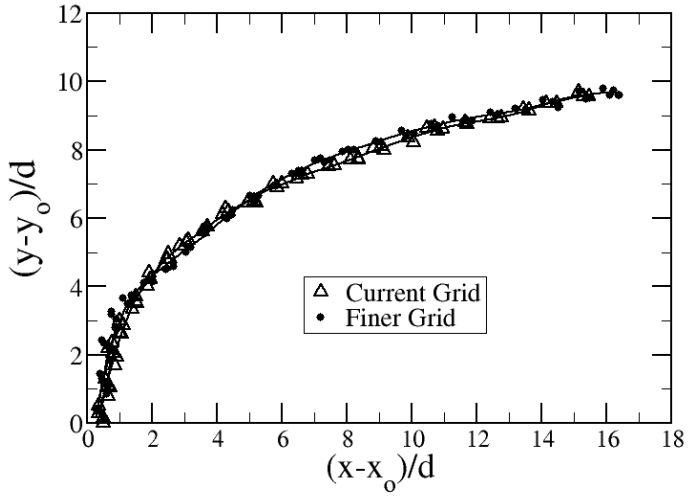

Figure 11: Comparison of normalized jet penetration with normalized distance from the injector, for Case 7.

parameters.

Physically, if the pulses were coming out of a piston (or from an injector in experiments), the stroke ratio is equivalent to the 'push' given to each pulse. The pulse width τ and the spatial separation (quantified by the duty cycle α) govern the interaction among the successive flow structures. This effect on the near field structure of the jet in turn changes the far-field jet penetration.

As mentioned earlier, based on the stroke ratio the jet splits into two streams: a deep penetrating vortex puff and a trailing jet of fluid. The two-branch pulsed jet structure can be seen in the Fig. 7. The trailing jet acts as a steady jet in crossflow and is responsible for enhanced entrainment and distribution of vorticity, which results in a lesser penetration depth compared to the distinct vortex rings. Increasing the stroke ratio, gives rise to stronger trailing jets. For low-speed flows, the scaling relation for penetration of fully modulated incompressible pulsed jets in crossflow has been derived from the self similar scaling relations of turbulent vortex rings and puffs in

quiescent media [8, 14, 13]

$$y - y_o = k \left[\frac{I}{\rho}(t - t_o) \right]^{1/4} \tag{24}$$

where I is the jet impulse at the nozzle exit. Assuming non-interacting vortex puffs drifting in the crossflow direction ($x = U_o(t - t_o)$), an incompressible scaling law for uniform density pulsed jets in crossflow is obtained as [17]

$$\frac{y - y_o}{d} = k \left(r_p \frac{L}{d} \right)^{1/4} \left(\frac{x}{d} \right)^{1/4} \tag{25}$$

where $r_p = \frac{\bar{U_j}}{U_{cf}}$ is the jet to crossflow velocity ratio of the pulse, y_o and t_o are virtual origin in space and time. The constant k is experimentally determined and is a function of various flow properties such as kinematic viscosity [13] and crossflow velocity profile. For a vortex puff, Richards [26] predicts $k = 2$ for an axial puff and $k = 3$ for a cylindrical puff.

Cases 6 and 7 are compared with experiments. Figure 12(a) shows the comparison between the LES data and the model, which has been used with a value of $k = 3.0$. The value of k obtained from the simulations is 3.02. In Fig. 12, the symbols are from the LES simulation and the straight lines are the expected values for the normalized jet penetration (from the scaling laws). For variable density jets, we now define an effective velocity ratio, r_e, as

$$r_e = \left(\frac{\rho_j U_j^2}{\rho_{cf} U_{cf}^2} \right)^{1/2} \tag{26}$$

and using the same approach as in Johari *et al.* [17], for variable density flows, we obtain

$$\frac{y - y_o}{d} = k \left(\sqrt{\frac{\rho_j U_j^2}{\rho_{cf} U_{cf}^2}} \frac{L}{d} \right)^{1/4} \left(\frac{x}{d} \right)^{1/4} \tag{27}$$

This scaling law is plotted in Fig. 12(b) for Cases 7, 8 and 9. In these cases, the velocity ratios and Strouhal numbers are the same. The change in jet to crossflow density ratios gives rise to different momentum ratios. Clearly, the new scaling law is

reasonably reproduced by the current simulations. The value of the constant, k, for the variable density jets is nearly the same as the k for the iso-density jets.

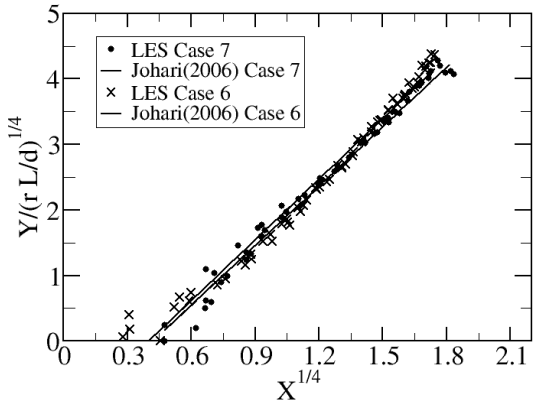

(a)

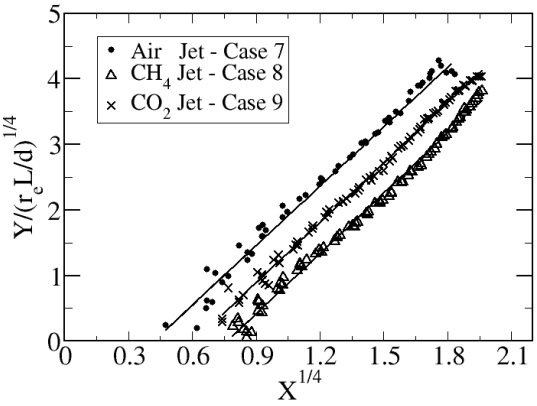

(b)

Figure 12: (a) Constant density scaling law [17] compared with current cases. Here, x and y are measured from the virtual origin. (b) Variable density scaling law validation , where $r_e = \left(\frac{\rho_j U_j^2}{\rho_o U_{cf}^2}\right)^{1/2}$, $Y = \frac{y}{d}$ and $X = \frac{x}{d}$

3.4 Passive Scalar Mixing

A maximum in jet penetration does not necessarily mean more mixedness [29]. Mixing depends on stroke ratio - in the sense that for lower stroke ratios ($3.6 \leq L/D \leq 4.5$),

more distinct vortex rings are formed and hence the expectation of more mixing. Passive scalar mixing of pulsed jets in crossflow is quantified by the decay of statistically averaged centerline jet concentration and is shown in Fig. 13. Here, Cases 7, 10 and 11 are used for this analysis. Since, CH_4 is the lightest of the three jets it mixes much more rapidly with the crossflow when compared to the other heavier jets. This translates to a much quicker decay in the jet concentration as seen in Fig. 13(a). In addition, we can also observe that the potential core of the CH_4 jet is $1d$ long, which is considerably shorter than the other jets. In Fig. 13(a), the symbols are from the LES simulation and the straight lines are the expected concentration decays from a scaling law that is based on the work of Johari [17].

He assumes that the mixing of the jet scales the same way as that of a turbulent puff. He thus approximates the decay of the centerline jet concentration as:

$$C(x) \sim r^{-3/4}(L/d)^{1/4}(x/d)^{-3/4} \tag{28}$$

For the CH_4 and CO_2 jets, we use the effective velocity ratio, r_e from eqn 26. Perfect agreement between the LES results and the scaling law cannot be expected, as the scaling is an approximation.

Figure 13(b) shows the dependence of the puff width, δ along the x axis. For a turbulent puff, Diez *et al.* [5] predict that the puff width depends on y as:

$$\delta \sim 0.24(y - y_o) \tag{29}$$

Using the variable density scaling law for $y - y_o$, we get

$$\frac{\delta}{d} \sim \left(r_e \frac{L}{d}\right)^{1/4} \left(\frac{x}{d}\right)^{1/4} \tag{30}$$

For Cases 7, 10 and 11, the effective velocity ratio, r_e, and the stroke ratio, $\frac{L}{d}$, are the same. This indicates the influence of the jet to crossflow density ratio on the jet spread. For steady jets, the mass flux defined by $\dot{m} = \rho u \delta^2$ gives the dependence of

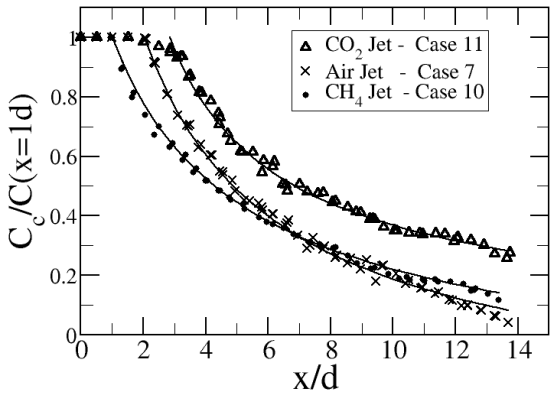

(a)

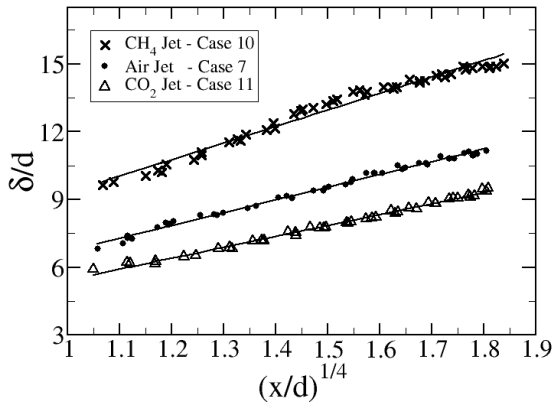

(b)

Figure 13: (a) Decay of the concentration of the jet (normalized by the value at x =1d) along the jet centerline (b) Variation of the total width, δ of the jet, along the x direction.

the jet spread as $\delta \propto \left(\frac{\rho_{cf}}{\rho_j}\right)^{1/2}$ [7]. Defining mass flux for turbulent puffs in a similar manner, we get an expression for the jet spread as:

$$\frac{\delta}{d} \sim \left(\frac{\rho_{cf}}{\rho_j}\right)^{1/2} \left(r_e \frac{L}{d}\right)^{1/4} \left(\frac{x}{d}\right)^{1/4} \tag{31}$$

In Fig 13(b), we can see that the jet spread scales as $(x/d)^{1/4}$. Again, CH_4 being the lightest of the three jets, shows the maximum jet spread and the CO_2 jet shows the minimum spread.

3.4.1 Mixing of Jet Species Without Flapping

The above results are recorded from the statistically averaged data. This requires an elimination of the possibility of jet concentration decay and the jet spread due to flapping, as opposed to mixing. Fig. 14 shows the instantaneous decay of the CH_4, Air and CO_2 jets from Cases 7, 10 and 11. CH_4 jet has a quicker concentration decay compared to the other jets, as the lower density jet diffuses easily into the crossflow. This has been observed in the statistically averaged concentration decay earlier and is now supported by the instantaneous data.

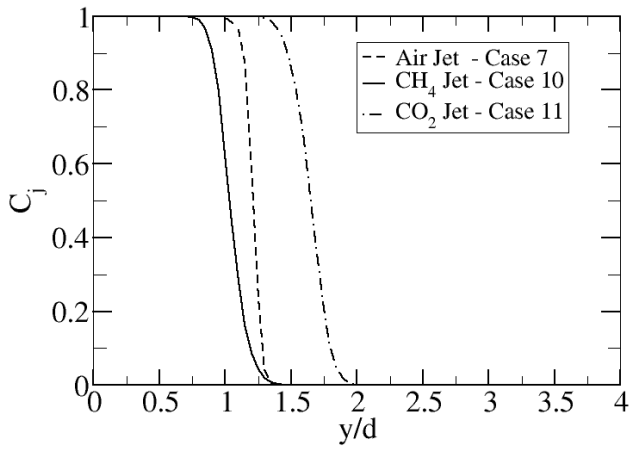

Figure 14: Instantaneous decay of jet concentration, where the $x-$ axis is the perpendicular distance from the center of the injector.

Fig 15 is used to show the absence of flapping of the jet for two consecutive pulses. Five instants in each pulse cycle are shown. The second pulse follows a path that is very much close to the first pulse. This shows that the predicted concentration decays are due to mixing, and not due to flapping.

Fig 16 shows the gradient ($|\bigtriangledown Y_{jet}|$) of the jet mass fraction for Case 10. Very high gradients in the shear layer between the jet and the crossflow is another indication that the decay in the jet concentration is due to jet-crossflow mixing.

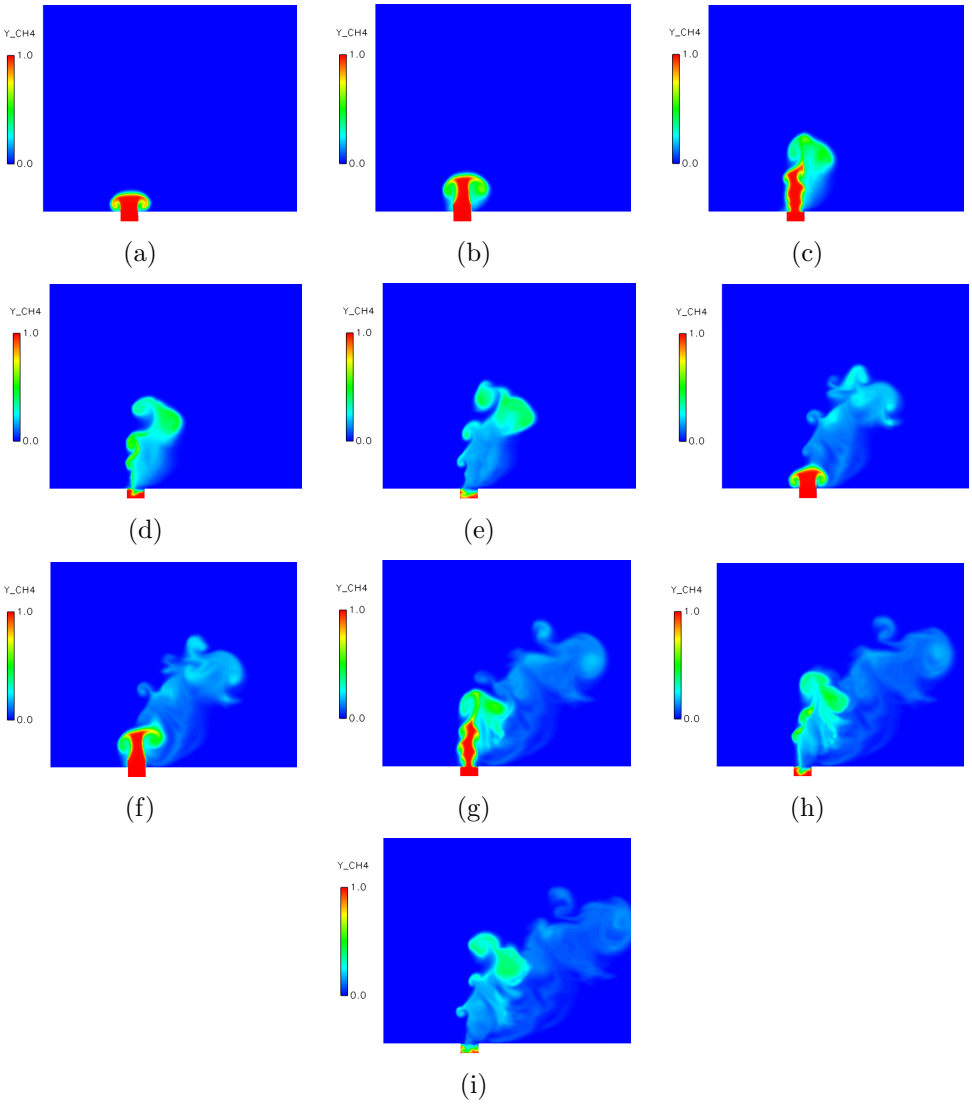

Figure 15: Contours of mass fraction of CH_4 jet for two consecutive pulses (Case 10). Figs (a) - (e) show images of the first pulse and Figs (f) - (i) show images of the next pulse.

3.5 Heated Jets

This study deals with two main aspects of heated jets - change in jet penetration scaling laws due to high temperatures and mixing of temperature between jet and crossflow. The incompressible scaling law, Eqn 25 has been derived from Eqn 24, which in turn has been derived from the dimensional analysis of an incompressible streamfunction

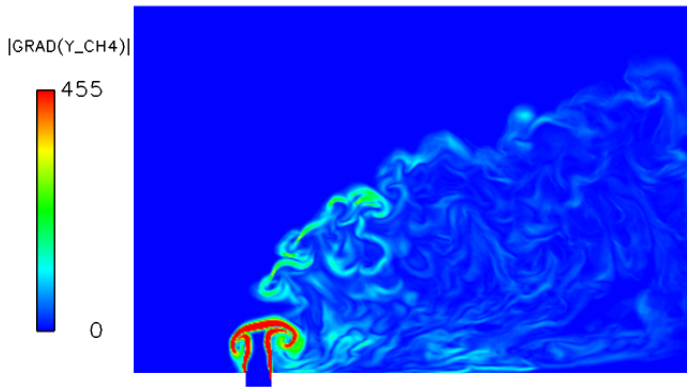

Figure 16: Contour of $|\bigtriangledown Y_{CH_4}|$ for Case 10, where Y_{CH_4} is the mass fraction of the CH_4 jet.

$$u = \frac{1}{r}\frac{\partial \psi}{\partial r}, \quad v = -\frac{1}{r}\frac{\partial \psi}{\partial x} \tag{32}$$

We begin with the compressible streamfunction for axisymmetric motion, so that

$$\rho u = \frac{1}{r}\frac{\partial \psi}{\partial r}, \quad \rho v = -\frac{1}{r}\frac{\partial \psi}{\partial x} \tag{33}$$

where ψ is the streamfunction that is dependant on three independent variables:

$$\psi = \psi(x, r, t) \tag{34}$$

If L, M and T are the parameters that define characteristic global length, mass and time scales respectively, the equation above can be restated as

$$\frac{\psi T}{M} = f\left(\frac{x}{L}, \frac{r}{L}, \frac{t}{T}\right) \tag{35}$$

For a vortex ring, we consider the three parameters I, ρ and ν, which define the moment of the inertia, density and kinematic viscosity of the ring respectively:

$$[I] = ML/T, \quad [\rho] = M/L^3, \quad [\nu] = L^2/T \tag{36}$$

Solving simultaneously for M, L and T from the above equations, we get

$$M = \rho \left(\frac{I}{\rho\nu}\right)^{3/2}, \quad L = \left(\frac{I}{\rho\nu}\right)^{1/2}, \quad T = \frac{1}{\nu}\left(\frac{I}{\rho\nu}\right) \tag{37}$$

Inserting the above forms of M, L and T into the dimensionless Eqn 35, we get:

$$\frac{\psi}{(\rho\nu I)^{1/2}} = f\left(x\left(\frac{\rho\nu}{I}\right)^{1/2}, r\left(\frac{\rho\nu}{I}\right)^{1/2}, \frac{t\rho\nu^2}{I}\right) \tag{38}$$

In the earlier incompressible analysis, each variable is multiplied by an appropriate power of $t\rho\nu^2/I$ (a non-dimensional variable) in order to eliminate the viscosity. However, we multiply each variable with an appropriate power of $t\rho\nu^2/I$ that includes the effects of the kinematic viscosity, ν

$$\psi = \nu^{1/8} f\left(x\left(\frac{\rho}{It}\right)^{1/4}, r\left(\frac{\rho}{It}\right)^{1/4}\right) \tag{39}$$

Equation 39 is in the form which has been used to derive the incompressible scaling law [17]. Adding the effect of viscosity in the self similar scaling for turbulent vortex puffs in crossflow (eqn 24) we get

$$y - y_o = k\frac{1}{\nu^{1/8}}\left[\frac{I}{\rho}(t - t_o)\right]^{1/4} \tag{40}$$

Hence, from the compressible scaling law, Eqn 27 and the dimensionless Eqn **??**, we get:

$$\frac{y - y_o}{d} = k\left(\frac{\nu_{cf}}{\nu_j}\right)^{0.125}\left(\sqrt{J}\frac{L}{d}\right)^{1/4}\left(\frac{x - x_o}{d}\right)^{1/4} \tag{41}$$

Equation 41 suggests that heated jets have a lower jet penetration, compared to jets with the same momentum ratio. This is attributed to increased kinematic viscosity at higher temperatures, which in turn causes higher dissipation of the jet momentum. The scaling law given in Eqn 41 can be simplified using $\nu = \mu/\rho$. The resulting equation agrees with the experimental observations of Callaghan *et al.* [2, 3] (Eqn 7), that the scaling law for heated jets depends on the mass flux ratio, as opposed to momentum ratio. It should, however, be noted that this is valid only for heated jets with the same jet and crossflow species, while the earlier variable density scaling (eqn

27) is valid for unheated jets with different jet and crossflow species.

Further validation of Eqn 41 can be seen in Fig 17. Cases 7, 12 and 13 have been used to validate the heated jet scaling law. A plot of $Y/(r_e L/d)^{1/4}$ eliminates the dependence of the jet penetration on the stroke and momentum ratio of the jet. Thus, the effect of a heated jet can be seen in decreasing k. The value of k for Case 12 is 2.67 and Case 13 is 1.6, which agree well with Eqn 41.

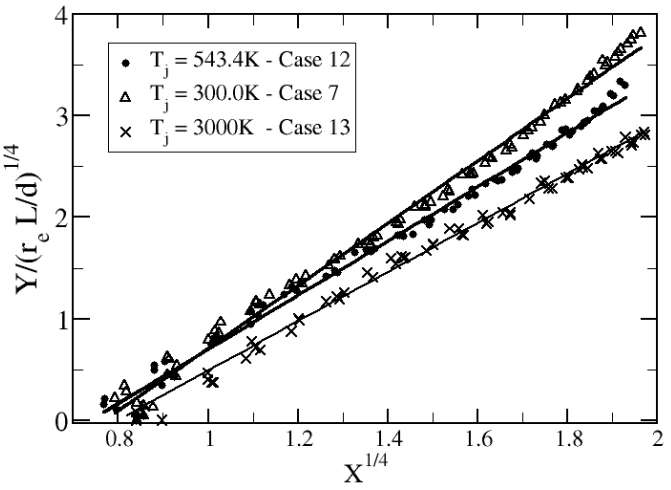

Figure 17: Variation of normalized penetration depth with normalized distance from the injector, for heated jets, where $r_e = \left(\frac{\rho_j U_j^2}{\rho_o U_{cf}^2}\right)^{1/2}$, $Y = \frac{y}{d}$ and $X = \frac{x - x_o}{d}$.

Heated jet applications are seen in ignition studies, where a hot kernel is to be mixed with fuel and oxidizer, in the main flow. In such applications, the presence of high temperatures in the crossflow is enough to cause ignition. This aspect is not captured by the statistically averaged temperature data (Fig 18(a)). At a given point in the domain, the 'on' and 'off' nature of the pulses, lowers the average temperature. Hence, more complex stochastic variables need to be used for mixing analysis of heated jets. The maximum possible temperature experienced at each point in the domain, would give an idea of the extent to which the influence of the heated jet is

seen in the domain. This is shown in Fig 18(b). It should be noted that the maximum temperature is computed over regular intervals of time and not at every time instant.

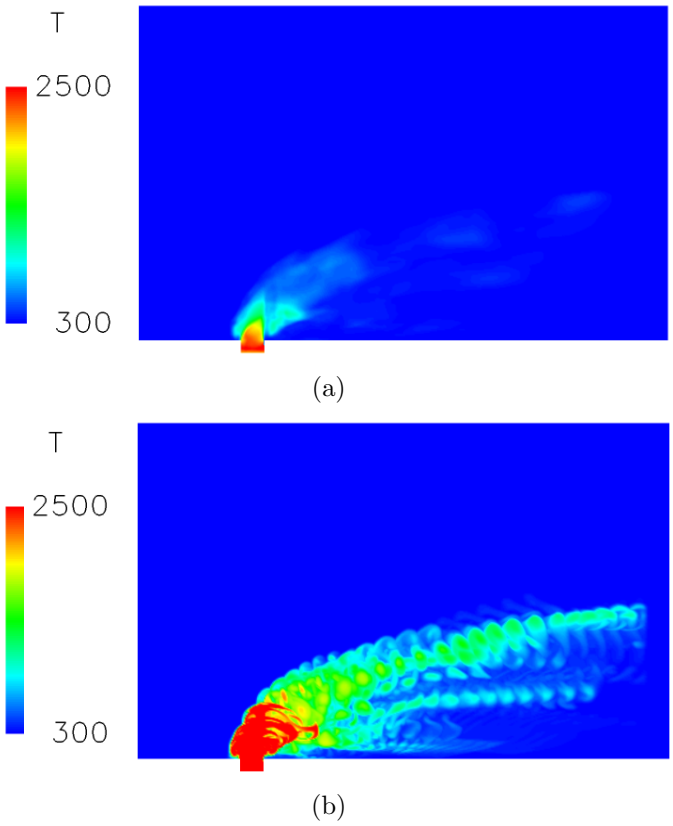

Figure 18: Temperature profiles for Case 13 (a) Statistically averaged temperature profile (b) Temperature profile showing the maximum possible temperature that each point experienced.

Temperature distributions in cross planes are studied using a dimensionless temperature:

$$\bar{\theta} = \frac{T - T_{cf}}{T_{max} - T_{cf}} \tag{42}$$

where T_{cf} is the temperature of the crossflow and T_{max} is the maximum temperature in a given normal plane. Figures 19 and 20 show contours of $\bar{\theta}$ for Cases 12 and 13, at two axial locations respectively.The black square box seen in the figures is the top view of the injector. In both cases, for $x/d = 1d$, we observe that the temperature diffuses quickly into the vortex region. Case 12 has a higher momentum ratio compared to Case 13, and hence we observe a stronger vortical action in the

temperature distribution for Case 12. Figures 19(b) and 20(b) suggest that the temperature maxima is observed near the vortex centers, and not necessarily on the plane of symmetry. In addition, the counter-rotating vortex pairs exist much deeper into the crossflow for the higher momentum ratio case. Finally, Fig 20(b) shows that the jet has moved away from the injector at $x/d = 2d$, whereas this is not the observation in fig 19(b). This, again, is a confirmation of the greater jet spread for higher momentum ratio jets.

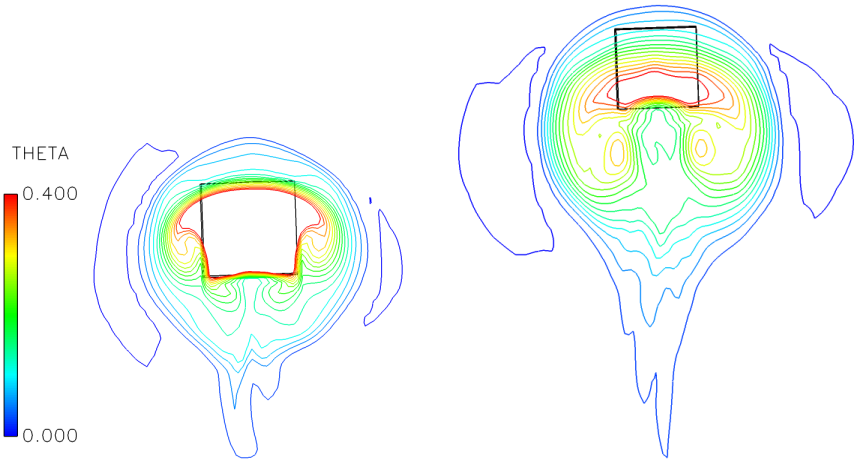

(a) (b)

Figure 19: Contours of constant temperature along the cross-section of the jet (Case 12). Figures show $x - z$ view. (a) $y/d = 1d$ (b) $y/d = 2d$

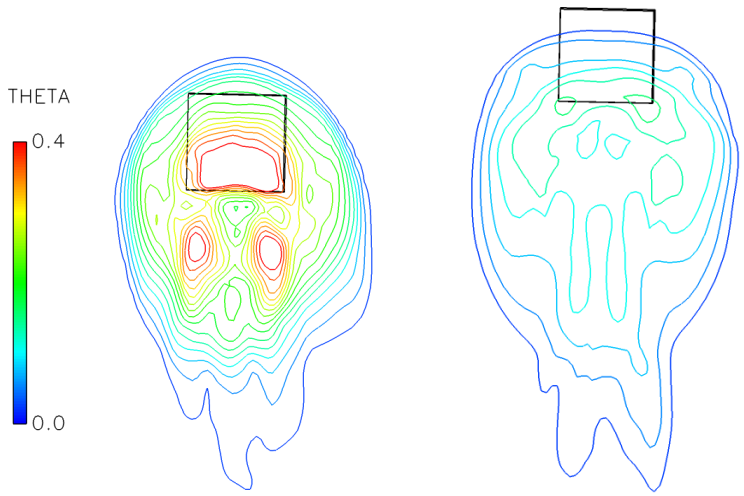

(a) (b)

Figure 20: Contours of constant temperature along the cross-section of the jet (Case 13). Figures show $x - z$ view. (a) $y/d = 1d$ (b) $y/d = 2d$

CHAPTER IV

CONCLUSIONS AND RECOMMENDATIONS

An LES simulation has been setup to study variable density pulsed jets in high speed crossflow. A crossflow with inflow turbulence has been developed and grid independent studies have been done. This is a new capability that has been developed for future use. The jet structure is qualitatively described by analysis of the flow features such as jet shear vortices, wake vortices and counter-rotating vortex pairs. Merging patterns of consecutive vortices is explicitly shown for distinct vortex puffs and vortices with trailing jets of fluid. For vortices with trailing jets, it is observed that the consecutive vortices first merge with the detached trailing edge before merging with the earlier pulse. Jet penetration is quantitatively compared with experiments and an iso-density scaling law. For variable density jets, it has been observed that the jet-to-crossflow density ratio needs to be considered in formulations jet penetration scaling law.

The effect of density ratios on mixing, is quantified by the decay of the scalar concentration along the jet centerline. It is shown that the lighter jet mixes, and hence decays much quicker, compared to the denser jets. Near field showed quicker decay (and hence faster mixing) compared to the far field. Higher mixing of the CH_4 jet has also resulted in greater jet spread. The jet spread, in turn has been quantified with a new variable density scaling law.

Heated jets for two different temperatures have been analyzed. The effect of kinematic viscosity of the scaling has been quantified. It has been observed that jets with higher temperatures have lower jet penetration due to increased viscosity, and this follows a $1/\nu^{0.125}$ dependence. In addition, temperature distributions, in the jet

Table 2: Summary of the scaling constants obtained from the iso-density, variable-density and heated jet scaling laws.

Case	$\rho_j/\rho_{cf}(M.Wt)$	$\rho_j/\rho_{cf}(T_{cf}/T_j)$	k	Ref Eqn. #
7	1.0	1.0	3.02	25
8	0.554	1.0	3.03	27
9	1.52	1.0	3.02	27
12	1.0	0.554	2.67	41
13	1.0	0.1	1.6	41

cross-section, have been studied for different momentum ratios.

In summary, the scaling results have been summarized in the Table 2:

In conclusion, the created simulation setup can be used to study the physics of high speed pulsed jets in turbulent crossflow. The simulation has been qualitatively validated by observing characteristic vortical features and is quantitatively validated with iso-density jet penetration studies. Existing iso-density scaling law has been extended to a variable density scaling law and a heated jet scaling law. With this existing work, the following issues can be studied in future:

- In addition to merging characteristics of consecutive pulses, the trailing edge behind each pulse further breaks into smaller vortices and is showing distinct merging patterns. This behavior can be further studied to obtain a classification map that provides the vortex shapes for variable density jets.

- The effect of St on the jet penetration and mixing has been studied for unheated jets. In a similar way, St also effects temperature mixing. A study of the sensitivity of temperature mixing to change in St, obtaining the optimum St for maximum mixing and comparing this to the optimum St of unheated jets, would give an insight into the conditions that would result in good mixing of temperature and scalar concentration of the jet with the crossflow.

- In steady jets, jet penetration defined by the maximum temperature along the jet is lower than that defined by the maximum velocity along the jet. This characteristic is also observed in pulsed jets. The jet trajectory based on temperature can similarly be analyzed for its scaling characteristics. This would give an idea of the temperature distribution as opposed to the velocity distribution.

- Combustors inject fuel into the crossflow for ignition. Hence, a study of reacting jets into crossflow provides an understanding of the ignition and flame characteristics for this configuration.

REFERENCES

[1] Broadwell, J. and Breidenthal, R., "Structure and mixing of a transverse jet in an incompressible flow," *J. of Fluid Mechanics*, vol. 148, pp. 405–412, 1984.

[2] Callaghan, E. and Ruggeri, R., "Investigation of the penetration of an air jet directed perpendicularly to an air stream," Tech. Rep. 1615, National Advisory Committee for Aeronautics, 1948.

[3] Callaghan, E. and Ruggeri, R., "A general correlation of temperature profiles downstream of a heated jet directed perpendicularly to an air stream," *NACA*, 1951.

[4] Chakravarthy, V. and Menon, S., "Large-eddy simulations of turbulent premixed flames in the flamelet regime," *Combustion Science and Technology*, vol. 162, pp. 175–222, 2001.

[5] Diez, F.J., B. L. and Faeth, G., "Round turbulent thermals, puffs, starting plumes and starting jets in uniform crossflow," *Journal of Heat Transfer*, vol. 125, pp. 1046–1057, 2003.

[6] Dubief, Y. and Delcayre, F., "On coherant-vortex identification in turbulence," *J. Turbulence*, pp. 1–22, 2000.

[7] Ernest, F, A. and Mungal, M., "Transverse jets and jet flames, part 1. scaling laws for strong transverse jets," *J. Fluid Mechanics*, vol. 443, pp. 1–25, 2001.

[8] Eroglu, A. and Breidenthal, E., "Structure, penetration, and mixing of pulsed jets in crossflow," *AIAA Journal*, vol. 39, pp. 417–423, 2001.

[9] Fric, T. and Roshko, A., "Vortical structure in the wake of a transverse jet," *J. of Fluid Mechanics*, vol. 279, pp. 1–47, 1994.

[10] Genin, F. and Menon, S., "Simulation of turbulent mixing behind a strut injector in supersonic flow," *47th AIAA Aerospace Sciences Meeting, Orlando, FL*, vol. 132, 2009.

[11] Genin, F., *Study of Compressible Turbulent Flows in Supersonic Environment by Large-Eddy Simulation.* PhD thesis, Georgia Institute of Technology, 2009.

[12] Genin, F. and Menon, S., "Dynamics of sonic jet injection into supersonic crossflow," *Journal of Turbulence*, vol. 11, pp. 1–30, 2010.

[13] Glezer, A., "The formation of vortex rings," *Phys. Fluids*, vol. 31, pp. 3532–3542, 1981.

[14] Glezer, A. and Coles, D., "An experimental study of a turbulent vortex ring," *J. Fluid Mechanics*, vol. 211, pp. 243–283, 1990.

[15] Hermanson, J., Wahba, A., and Johari, H., "Duty-cycle effects on penetration of fully modulated, turbulent jets in crossflow," *AIAA J*, vol. 36, pp. 1935–1937, 1998.

[16] Jiang, X. and Luo, K., "Direct numerical simulation of the puffing phenomenon of an axisymmetric thermal plume," *Theoret. Comput. Fluid Dynamics*, vol. 14, pp. 55–74, 2000.

[17] Johari, H., "Scaling of fully pulsed jets in crossflow," *AIAA Journal*, vol. 44, pp. 2719–2725, 2006.

[18] Johari, H., Pacheco-Tougas, M., and Breidenthal, E., "Penetration and mixing of fully modulated turbulent jets in crossflow," *AIAA Journal*, vol. 37, pp. 842–850, 1999.

[19] Kamotani, Y. and Greber, I., "Experiments on a turbulent jet in a crossflow," *AIAA Journal*, vol. 10, pp. 1425–1429, 1972.

[20] Kim, W. and Menon, S., "A new incompressible solver for large eddy simulations," *International Journal of Numerical Fluid Mechanics*, vol. 31, pp. 983–1017, 1999.

[21] Krueger, P. and Gharib, M., "Thrust augmentation and vortex ring evolution in a fully pulsed jet," *AIAA J*, vol. 43, pp. 792–801, 2005.

[22] Lester L. Yuan, R. L. S., "Trajectory and entrainment of a round jet in crossflow," *Physics of Fluids*, vol. 10, pp. 2323–2335, 1998.

[23] M'Closkey, R., King, J., Cortelezzi, L., and Karagozian, A., "The actively controlled jet in crossflow," *J. Fluid Mechanics*, vol. 452, pp. 325–335, 2002.

[24] Menon, S. and Patel, N., "Subgrid modeling for simulation of spray combustion in large-scale combustors," *AIAA Journal*, vol. 44, pp. 709–723, 2006.

[25] Ramsey, J. W. and Goldstein, R., "Interaction of a heated jet with a deflecting stream," *ASME Journal of Heat Transfer*, vol. 93, pp. 365 – 372, 1971.

[26] Richards, J., "Puff motions in unstratified surroundings," *J. Fluid Mechanics*, vol. 21, pp. 97–106, 1965.

[27] Sau, R. and Mahesh, K., "Dynamics and mixing of vortex rings in crossflow," *J. Fluid Mech*, vol. 604, pp. 389–409, 2008.

[28] Sau, R. and Mahesh, K., "Optimization of pulsed jets in crossflow," *47th AIAA Aerospace Sciences Meeting, Orlando, Florida*, 2009.

[29] Shapiro, S., King, J., Closkey, R., and Karagozian, A., "Optimization of controlled jets in crossflow," *AIAA J*, vol. 44, pp. 1292–1298, 2006.

[30] Smith, S. and Mungal, M., "Mixing, structure and scaling of the jet in crossflow," *J. of Fluid Mechanics*, vol. 357, pp. 83–122, 1998.

[31] Suman, M. and Mahesh, K., "Study of trajectories of jets in crossflow using direct numerical simulations," *J. Fluid Mech*, vol. 530, pp. 81–100, 2005.

[32] Vermeulen, P., Chin, C., and Yu, W., "Mixing of an acoustically pulsed air jet with a confined crossflow," *J. Propulsion and Power*, vol. 6, pp. 777–783, 1990.

[33] Vermeulen, P., Grabinski, P., and Ramesh, V., "Mixing of an acoustically excited air jet with a confined hot crossflow," *35th International Gas Turbine and Aeroengine Congress and Exposition*, vol. 114, pp. 46–54, 1992.